J. Fluid Mech. (2023), *vol.* 966, A17, doi:10.1017/jfm.2023.420

Translational and angular velocities statistics of inertial prolate ellipsoids in a turbulent channel flow up to $Re_\tau = 1000$

Antoine Michel[1] **and Boris Arcen**[1,†]

[1]Université de Lorraine, CNRS, LEMTA, F-54000 Nancy, France

(Received 2 August 2022; revised 3 May 2023; accepted 5 May 2023)

Direct numerical simulations of the turbulent flow in a channel are conducted up to $Re_\tau = 1000$ to examine the influence of the friction Reynolds number on the translational and angular velocities of inertial, prolate ellipsoids. The quadrant distribution of the turbulent events seen by the particles is not significantly affected by the value of Re_τ, but subtle modifications take place, depending on the position in the channel and on the particle relaxation time. Overall, the influence of Re_τ on the first and second statistical moments of the ellipsoids translational velocity is the same as that observed for the fluid velocity. The weak dependence of these statistics to the particle shape previously observed at low Reynolds number remains at higher values of Re_τ. Similarly, the mean and root mean square (r.m.s.) of the angular velocity of the fluid seen by the particles weakly depend on particle shape and they have the same dependence to Re_τ as the angular velocity statistics of the carrier fluid. Particle angular velocity statistics are more strongly affected by the flow Reynolds number due to the evolution of the complex shape and inertia dependent rotation orbits with Re_τ. In the near-wall region the average angular velocity of weakly inertial ellipsoids increases with Re_τ due to their stronger alignment with the mean fluid vorticity. Furthermore, the r.m.s. of the wall-normal component of the angular velocity of more inertial ellipsoids increases with Re_τ owing to the larger fluctuations of the angle between the particle major axis and the velocity-gradient plane.

Key words: channel flow, multiphase flow, turbulence simulation

1. Introduction

The dynamics of particles in turbulent flows is of interest to understand a wide variety of natural phenomena, ranging from the dispersion of plankton in the marine environment (Font-Muñoz *et al.* 2015) to the formation of ice crystals in mixed phase clouds (Naso *et al.* 2018), as well as to optimize industrial processes such as papermaking (Lundell, Söderberg

† Email address for correspondence: boris.arcen@univ-lorraine.fr

© The Author(s), 2023. Published by Cambridge University Press

https://doi.org/10.1017/jfm.2023.420 Published online by Cambridge University Press

& Alfredsson 2011). Non-spherical particles can be modelled by spheroids, and provide a better understanding of the two-phase flow characteristics than a spherical model (Voth & Soldati 2017). The challenge encountered in predicting the behaviour of such flows is linked to the particle shape, whose interaction with the fluid velocity and velocity-gradient fields results in complex translational and rotational dynamics.

Several experimental studies have been dedicated to understand the influence of turbulent fluid motion on particle orientation. For example, Bernstein & Shapiro (1994) observed that long fibres align along the mean velocity in a laminar duct flow, but did not observe this preferential alignment if the flow is turbulent. Parsheh, Brown & Aidun (2005) analysed the influence of the turbulent intensity on the preferential orientation of rigid fibres in a planar contraction and concluded that preferential orientation is controlled by the mean velocity gradient rather than by the turbulent intensity. In an open channel, Abbasi Hoseini, Lundell & Andersson (2015) observed that the preferential orientation relative to the mean flow and the turbulent events sampled by weakly inertial fibres strongly depends on their length. Capone, Felice & Pereira (2021) noted a peak in the concentration of nylon fibres at a wall distance equivalent to half the particle length in a turbulent channel flow at $Re_\tau = 530$ (based on the wall-shear velocity u_τ and the channel half-width δ), and reported that the mean angle between the fibres and the streamwise direction strongly varied with the distance from the wall. Shaik *et al.* (2020) measured the orientation and angular velocity of long, rigid nylon fibres (having an aspect ratio of 30.7 and 47) in a turbulent channel flow at $Re_\tau = 435$. They found that the average orientation of such particles weakly depends on their length, but that longer particles exhibit higher tumbling rates. Alipour *et al.* (2021) reported a moderate influence of curvature on the orientation and angular velocity of weakly inertial, flexible rods at $Re_\tau = 360$. Finally, Baker & Coletti (2022) measured the preferential orientation and the tumbling rate of long (50 in wall units), inertial fibres in a turbulent channel flow at $Re_\tau = 620$. They observed that the fibres major axis is preferentially aligned with the mean flow in the near-wall region, but that high tumbling rates occur intermittently due to the effect of the mean shear, the turbulent fluid velocity fluctuations and the particle–wall interactions.

Besides experimental studies, numerical simulations have proved to be a powerful tool to study the dynamics of non-spherical particles in a turbulent channel flow. The pioneering study of Zhang *et al.* (2001) introduced a methodology based on direct numerical simulation (DNS) of the turbulent flow coupled with Lagrangian tracking of ellipsoidal particles, treated as material points under a one-way coupling assumption. Such a method requires modelling the force and torque applied by the flow on the ellipsoids. This is generally done by the theoretical formulas of Happel & Brenner (1965) for the force and Jeffery (1922) for the torque. Such formulas have been successfully used to reproduce the orientational dynamics of weakly inertial rods in homogeneous isotropic turbulence (Parsa *et al.* 2012). This methodology was later extended to simulate more complex systems, such as dense suspensions where two-way (Zhao, Andersson & Gillissen 2013) and four-way (van Wachem *et al.* 2015; Zhao, George & van Wachem 2015*a*) coupling effects are important, or to model flexible fibres (Dotto, Soldati & Marchioli 2019). To focus on the effect of turbulence on the particle dynamics, one-way particle–fluid coupling is adopted in the present study: the effect of the particle on the fluid flow is supposed negligible as well as the interparticle interactions.

In their study, Zhang *et al.* (2001) simulated the turbulent flow in a channel at a friction Reynolds number $Re_\tau = 125$ to study the deposition of fibres modelled as prolate ellipsoids. Marchioli, Fantoni & Soldati (2010) worked with a somewhat similar $Re_\tau = 150$ and provided additional orientation and translational velocity statistics.

https://doi.org/10.1017/jfm.2023.420 Published online by Cambridge University Press

The same methodology was used by Mortensen *et al.* (2008*a*) to study the influence of the particle aspect ratio and inertia on translational velocity and angular velocity statistics in a turbulent channel flow at $Re_\tau = 180$. They found that translational velocity statistics are not significantly affected by particle shape, but that angular velocity statistics are strongly shape dependent in the near-wall region, where the mean velocity gradient causes periodic rotation of the ellipsoids. Marchioli, Zhao & Andersson (2016) analysed the relative rotation between the particle and fluid, and also noted an important influence of the aspect ratio. More recently, Zhao *et al.* (2019) mapped the ellipsoids rotation modes at different locations in the channel and noted that in the viscous sublayer the particles rotation plane depends on their aspect ratio and inertia. Finally, Challabotla, Zhao & Andersson (2016) and Arcen *et al.* (2017) noted a strong influence of gravity on the preferential orientation and concentration of inertial ellipsoids at $Re_\tau = 180$. These studies provided insight into the dynamics of inertial and ellipsoidal particles in a low-Reynolds-number turbulent channel flow.

Several groups also conducted studies at higher values of the Reynolds number. van Wachem *et al.* (2015) conducted four-way coupled large-eddy simulations of the flow in a horizontal channel at $Re_\tau = 600$. They analysed the particle shape effect, as well as the influence of the wall roughness. They notably found a significant effect on translational velocity statistics and concentration profiles. Ouchene *et al.* (2018) conducted DNS of the turbulent flow at $Re_\tau = 1440$ to study acceleration statistics of inertial ellipsoids. While they noted a significant effect of the particles aspect ratio on these statistics, they did not examine the effect of the flow Reynolds number. The influence of this parameter on the dynamics of ellipsoidal particles has only been examined in a few studies. Zhao, Marchioli & Andersson (2014) computed the mean and root mean square (r.m.s.) of the slip velocity of inertial ellipsoids at $Re_\tau = 150$, 180 and 300. They noted an increase of the magnitude of these properties, but did not generalize their conclusions to higher values of the flow Reynolds number. They indicated that simulations at higher values of the Reynolds number are required to confirm the influence of Re_τ on these statistics. Jie *et al.* (2019) used pre-computed DNS flow fields at $Re_\tau = 1000$ to examine the influence of this parameter on orientation and rotation statistics of inertialess ellipsoids in the channel core. They did not report an important effect of Re_τ on the preferential orientation, but observed a strong decrease of the ellipsoids rotation rate in the quiescent core at $Re_\tau = 1000$. In a recent communication, Michel & Arcen (2021*b*) examined the influence of Re_τ on the concentration profiles and orientation statistics of inertial ellipsoids. They noted that increasing the value Re_τ resulted in a stronger alignment between the particle major axis and vorticity vector in the channel core, as well as in a modification of the rotation orbits induced by Jeffery (1922)'s formula in the near-wall region, up to $Re_\tau = 550$. A uniformization of the ellipsoids concentration profile was also noted as the Reynolds number increases, in a manner similar to that observed for inertial spheres by Bernardini (2014).

Numerical studies of the translational and rotational dynamics of inertial spheroidal particles were mainly focused on the influence of the particle shape and inertia at low Reynolds numbers. The present study aims at gaining more insight into the influence of Re_τ on the statistical properties describing the translation and rotation of inertial ellipsoids in a turbulent channel flow. The methodology relies on DNS of the turbulent flow, coupled with Lagrangian particle tracking. To obtain reliable data, simulations are conducted until the particle distribution has reached a statistically steady state before computing the dispersed phase statistics (Michel & Arcen 2021*a*). Using this methodology, the concentration profiles and preferential orientation of inertial ellipsoids

https://doi.org/10.1017/jfm.2023.420 Published online by Cambridge University Press

were examined up to $Re_\tau = 550$ (Michel & Arcen 2021*b*). In the present study the dynamical quantities characterizing the interaction of the particles with the turbulent flow are analysed. Preferential concentration, translational velocity and angular velocity statistics are computed up to $Re_\tau = 1000$ to analyse the dynamics of inertial ellipsoids in a fully turbulent channel flow. The paper is organized as follows. Equations of fluid and particle motion are presented in § 2, followed by the numerical set-up and simulation parameters in § 3. To quantify the influence of Re_τ on the dispersed phase dynamics, statistics about preferential concentration, translational velocity and angular velocity are then presented. Quadrant analysis is performed in § 4 to quantify preferential concentration. Translational velocity statistics are described in § 5, and angular velocity statistics are presented in § 6. Finally, the main findings are summarized in § 7

2. Governing equations

2.1. *Fluid phase*

The turbulent flow is described by the continuity and momentum conservation equations for a Newtonian, incompressible and isothermal fluid,

$$\nabla \cdot \boldsymbol{u} = 0, \tag{2.1}$$

$$\frac{\partial \boldsymbol{u}}{\partial t} + (\boldsymbol{u} \cdot \nabla)\boldsymbol{u} = -\frac{1}{\rho_f}\nabla p + \nu \nabla^2 \boldsymbol{u}, \tag{2.2}$$

where $\boldsymbol{u}$ is the velocity field, p the pressure field, ρ_f the fluid density and ν the fluid kinematic viscosity.

2.2. *Lagrangian particle tracking*

Particles are modelled as prolate spheroids of aspect ratio $\lambda = a/b > 1$, a and b being the lengths of the semi-major and semi-minor axes. The particle position and orientation are obtained by solving the following sets of equations:

$$\frac{\mathrm{d}\boldsymbol{x}_p}{\mathrm{d}t} = \boldsymbol{u}_p, \quad m_p \frac{\mathrm{d}\boldsymbol{u}_p}{\mathrm{d}t} = \boldsymbol{F}, \tag{2.3a,b}$$

$$\frac{\mathrm{d}\boldsymbol{q}_p}{\mathrm{d}t} = \frac{1}{2}\boldsymbol{q}_p \boldsymbol{\omega}'_p, \quad \boldsymbol{I}_I \frac{\mathrm{d}\boldsymbol{\omega}'_p}{\mathrm{d}t} + \boldsymbol{\omega}'_p \times (\boldsymbol{I}_I \boldsymbol{\omega}'_p) = \boldsymbol{T}'. \tag{2.4a,b}$$

Here $\boldsymbol{x}_p$ and $\boldsymbol{u}_p$ are the particle position and translational velocity, while $\boldsymbol{q}_p$ and $\boldsymbol{\omega}'_p$ are the unit quaternion describing the orientation of the particle and particle angular velocity vector, respectively; $m_p = \rho_p (4/3)\pi a b^2$ is the particle mass, ρ_p denotes its density and $\boldsymbol{I}_I$ is the particle inertia tensor; $\boldsymbol{F}$ is the fluid force and $\boldsymbol{T}'$ the torque acting on the particle. Note that translation equations are solved in the Eulerian frame (x, y, z) while rotation equations are solved in the frame linked to the particle principal axes (x', y', z'). In this frame, the particle major axis is aligned with x'.

Particles are treated as material points, and the coupling between the fluid and particle phases is modelled and not directly solved. The force and torque models employed in the present study were obtained under the Stokes flow assumption. They are therefore valid if the particle Reynolds number $Re_p = d_{eq}\|\boldsymbol{u}_r\|/\nu \ll 1$, where $d_{eq} = 2b\sqrt[3]{\lambda}$ is the diameter of the volume equivalent sphere, and $\boldsymbol{u}_r = \tilde{\boldsymbol{u}} - \boldsymbol{u}_p$ is the relative velocity between the particle and the fluid, $\tilde{\boldsymbol{u}} = \boldsymbol{u}(\boldsymbol{x}_p, t)$ being the fluid velocity at the particle position. In addition, the mass density is assumed to be homogeneously distributed within each

https://doi.org/10.1017/jfm.2023.420 Published online by Cambridge University Press

particle. The additional gravitational torque that would arise in the presence of the gravity is therefore not considered. The force $\boldsymbol{F}$ is obtained by the formula from Happel & Brenner (1965),

$$\boldsymbol{F} = \nu\rho_f(\boldsymbol{A}^{-1}\boldsymbol{K}\boldsymbol{A})\boldsymbol{u}_r, \tag{2.5}$$

where $\boldsymbol{A}$ is the direction cosine matrix that is used to express vectors and tensors from the Eulerian frame in the particle frame. This matrix is computed knowing the particle orientation, as described in Zhang *et al.* (2001). Here $\boldsymbol{K}$ is the translational resistance tensor that describes the influence of particle shape on its translational motion. It is diagonal in the particle frame (x', y', z') and, for prolate spheroids, the components are (Gallily & Cohen 1979)

$$K_{x'x'} = \frac{8\pi b(\lambda^2 - 1)}{\left[\ln\left(\lambda + \sqrt{\lambda^2 - 1}\right)\dfrac{2\lambda^2 - 1}{\sqrt{\lambda^2 - 1}}\right] - \lambda}, \tag{2.6}$$

$$K_{y'y'} = \frac{16\pi b(\lambda^2 - 1)}{\left[\ln\left(\lambda + \sqrt{\lambda^2 - 1}\right)\dfrac{2\lambda^2 - 3}{\sqrt{\lambda^2 - 1}}\right] + \lambda}, \tag{2.7}$$

$$K_{z'z'} = K_{y'y'}. \tag{2.8}$$

Due to the product $\boldsymbol{A}^{-1}\boldsymbol{K}\boldsymbol{A}$, $\boldsymbol{F}$ can be decomposed as $\boldsymbol{F} = \boldsymbol{F}_D + \boldsymbol{F}_L$. Here $\boldsymbol{F}_D$ is the drag force, the component of $\boldsymbol{F}$ collinear to $\boldsymbol{u}_r$, while $\boldsymbol{F}_L$ is the lift force, the component of $\boldsymbol{F}$ orthogonal to $\boldsymbol{u}_r$. This lift force is induced by the particle anisotropy and orientation and it is not related to the shear-induced lift, for which an expression was recently derived by Cui *et al.* (2018). To retain the same framework as the one generally used (Mortensen *et al.* 2008*a*; Marchioli *et al.* 2010; Siewert, Kunnen & Schröder 2014*b*; Voth & Soldati 2017; Zhao *et al.* 2019), the shear-induced lift is not included.

With $\boldsymbol{F}$ known, the particle relaxation time can be obtained. It is the characteristic time required for a particle to adjust to a change in the flow characteristics. This time is not unique and several definitions are summed up by Siewert *et al.* (2014*a*). In the present study we use the definition from Shapiro & Goldenberg (1993), obtained by averaging $\boldsymbol{K}$ over an isotropic orientation distribution

$$\tau_p = \frac{2\lambda\rho_p b^2}{9\rho_f\nu}\frac{\ln(\lambda + \sqrt{\lambda^2 - 1})}{\sqrt{\lambda^2 - 1}}. \tag{2.9}$$

When expressed in wall units (using u_τ and ν), this is the particle Stokes number: the ratio of the particle relaxation time to the viscous time scale of the flow (ν/u_τ^2).

The torque is modelled with the formula from Jeffery (1922),

$$\boldsymbol{T}' = \frac{16\pi\mu ab^2}{3}\begin{pmatrix} \dfrac{1}{\beta_0}\left[(\Omega'_{zy} - \omega'_{px})\right] \\ \dfrac{1}{\beta_0 + \lambda^2\alpha_0}\left[(1-\lambda^2)S'_{xz} + (1+\lambda^2)(\Omega'_{xz} - \omega'_{py})\right] \\ \dfrac{1}{\lambda^2\alpha_0 + \beta_0}\left[(\lambda^2 - 1)S'_{yx} + (\lambda^2 + 1)(\Omega'_{yx} - \omega'_{pz})\right] \end{pmatrix}, \tag{2.10}$$

with μ the fluid dynamic viscosity and ω'_{pi} the components of the particle angular velocity. Here S'_{ij} and Ω'_{ij} are the fluid rate-of-strain tensor and rate-of-rotation tensor at particle

https://doi.org/10.1017/jfm.2023.420 Published online by Cambridge University Press

Re_b	Re_τ	L_x/δ	L_z/δ	N_x	N_y	N_z	Δ_x^+	Δ_y^+	Δ_z^+	Δt^+	$\eta_{k,min}^+$	$\eta_{k,max}^+$
2820	179	4π	1.33π	288	128	160	7.85	$0.98-4.44$	4.67	0.11	1.54	3.69
10 050	543	2π	1.33π	450	352	400	7.68	$1.08-4.94$	5.62	0.08	1.44	4.84
20 000	994	2π	π	768	448	512	8.17	$1.02-8.03$	6.09	0.07	1.41	5.58

Table 1. Value of the bulk Reynolds number and corresponding friction Reynolds number, domain size, number of mesh point, grid spacing, temporal increment. The minimum and maximum values of Kolmogorov's length scale, $\eta_{k,min}^+$ and $\eta_{k,max}^+$, were estimated using the data provided by Lee & Moser (2015). The superscript $+$ indicates a quantity expressed in wall units (normalized using u_τ and ν).

position, expressed in the particle frame (x', y', z'),

$$S'_{ij} = \tfrac{1}{2}\left(\partial u_i/\partial x_j + \partial u_j/\partial x_i\right)', \quad \Omega'_{ij} = \tfrac{1}{2}\left(\partial u_i/\partial x_j - \partial u_j/\partial x_i\right)'. \tag{2.11a,b}$$

By definition, the components of the rate-of-rotation tensor are directly linked to the vorticity by the formula

$$\Omega_{ij} = -\tfrac{1}{2}\epsilon_{ijk}\omega_k, \tag{2.12}$$

where ϵ_{ijk} is the Levi–Civita tensor. The explicit expression of α_0 and β_0 are given by Gallily & Cohen (1979). As previously explained, the present study is conducted in the same framework as the one generally used to examine the dynamics of inertial ellipsoids in a turbulent channel flow. The fluid inertia contribution is therefore neglected in the models of the hydrodynamic force and torque.

3. Simulation set-up

A finite difference DNS solver is used to compute the turbulent flow in a channel of width 2δ at three different Reynolds numbers. Periodic boundary conditions are applied in the x and z directions (statistically homogeneous directions) and a no-slip/no-penetration condition is enforced at $y = \pm\delta$. The numerical method is described by Michel & Arcen (2021*a*), only its main characteristics are presented hereafter. Similarly to the finite difference code used by Vreman & Kuerten (2014), the spatial derivatives appearing in (2.1) and (2.2) are approximated using fourth-order schemes in the streamwise and spanwise directions, while second-order schemes are used in the wall-normal direction. The time advancement is performed by a fully explicit third-order low-storage Runge–Kutta scheme (Le & Moin 1991), and the time step is obtained by fixing a constant Courant number of 0.5. At each Runge–Kutta stage, the pressure–velocity coupling problem is solved using the pressure-correction method proposed by Timmermans, Minev & van de Vosse (1996).

The mean flow is directed along x, and statistical stationarity of the turbulent flow is enforced by keeping the flow rate constant. The flow characteristics are therefore specified by fixing the bulk Reynolds number, $Re_b = U_b\delta/\nu$, based on the mean bulk velocity U_b. The associated friction Reynolds number, Re_τ, based on the wall-shear velocity, is computed *a posteriori*. Table 1 summarizes the values of Re_b used to obtain the three target friction Reynolds numbers, $Re_\tau = 180$, 550 and 1000, as well as the number of mesh points, grid spacing and averaged time step for each case. A preliminary study of the flow statistics has shown very good agreement with the statistics provided by Vreman & Kuerten (2014) for $Re_\tau = 180$, and by Lee & Moser (2015) for $Re_\tau = 550$ and 1000, respectively. The relative error on the mean and r.m.s. velocity and vorticity profiles did not exceed 1.5 %.

https://doi.org/10.1017/jfm.2023.420 Published online by Cambridge University Press

			ρ_p/ρ_f		
λ	a^+	b^+	$\tau_p^+ = 1$	$\tau_p^+ = 5$	$\tau_p^+ = 30$
1	0.50	0.50	18	90	540
3	1.04	0.35	20	100	601
10	2.32	0.23	27.8	139	833

Table 2. Characteristics of prolate spheroids. The volume equivalent sphere diameter is constant and equal to $d_{eq}^+ = 1$.

Particles are modelled as prolate spheroids. Three aspect ratios $\lambda = 1$, 3 and 10 are investigated as well as three relaxation times (2.9), in wall units $\tau_p^+ = 1$, 5 and 30. Particle geometry was chosen so that the volume equivalent sphere diameter remains constant. With this definition, the ratio of the major axis length to the minimal value of Kolmogorov's length scale, $2a^+/\eta_{k,min}^+$, is lower than 1 for $\lambda = 1$ for the three values of Re_τ considered in the present study. For the ellipsoids, the ratio $2a^+/\eta_{k,min}^+$ varies between 1.35 ($\lambda = 3$ and $Re_\tau = 180$) and 3.29 ($\lambda = 10$ and $Re_\tau = 1000$). Jeffery's formula (2.10) can be reasonably employed to compute the torque acting on ellipsoidal particles under this condition (Ravnik, Marchioli & Soldati 2018). The particle parameters are provided in table 2. To focus on the effect of turbulence on the particle dynamics, the particle–fluid coupling is one way: the effect of the particles on the fluid dynamics is supposed negligible as well as interparticle interactions. Therefore, the results presented in this study apply to the dilute limit of particle-laden flows. The particle volume fraction is a function of the number of particles introduced in the computational domain, and this number was selected in order to get reliable statistics in the time window studied and to keep the computational cost affordable. Periodic boundaries are applied to the dispersed phase in the streamwise and spanwise directions. Wall-particle collisions are treated as elastic when the distance between the particle centre of mass and the wall is smaller than $d_{eq}/2$. Note that the particle orientation is not accounted for in the rebound treatment, and that only the wall-normal component of the particle translational velocity is reversed when a collision occurs. This approximation is commonly used to study the dynamics of ellipsoids in a turbulent channel flow (Mortensen *et al.* 2008*a*; Zhao *et al.* 2015*b*; Ouchene *et al.* 2018; Zhao *et al.* 2019). The equations governing the ellipsoidal translational and rotational motions are solved with the same third-order low-storage Runge–Kutta scheme as used in the fluid solver. The time step used to integrate in time the particle equations of motion is also similar to that used in the fluid solver. Its value is obtained from the formula $\Delta t = \min(\Delta t_f,\ \Delta t_{p,1},\ \Delta t_{p,2})$, where Δt_f is the time step provided by the flow solver with the previously mentioned Courant–Friedrichs–Lewy (CFL) condition. Here $\Delta t_{p,1}$ and $\Delta t_{p,2}$ are additional time step restrictions imposed to solve the particle equations of motion; $\Delta t_{p,1} = \tau_p^s/10$, where $\tau_p^s = (\rho_p d_{eq}^2)/(18\rho_f \nu)$ is the spherical particle relaxation; $\Delta t_{p,2}$ is an equivalent CFL condition for the particle phase that prevents particles crossing over more than one cell in one time step. The averaged time step is provided in table 1. The fluid velocity and velocity gradient necessary to compute the hydrodynamic actions on each particle are interpolated at the particle position using a tricubic Hermite interpolation and a trilinear interpolation, respectively.

Here 300 000 prolate spheroids are seeded uniformly in the turbulent flow field. The particle translational and rotational velocities are initially equal to that of the fluid at their position, while their orientation is randomized.

https://doi.org/10.1017/jfm.2023.420 Published online by Cambridge University Press

After the particles are released in the turbulent flow, their metrics are collected every 200 iterations, corresponding to an average time interval of 18 in wall units. The same methodology as the one presented in Michel & Arcen (2021*a*) was used to avoid the statistical bias due to transient effects. First, the temporal evolution of the entropy parameter (Picano, Sardina & Casciola 2009) was computed to determine the time required by the particle distribution to reach a statistically steady state. Second, from this time, data were accumulated over an interval of duration of 20 000 in wall units to ensure that the sample used to compute statistics is large enough to be representative, even in regions of low particle concentration. For all three values of Re_τ, the distribution of $\tau_p^+ = 1$ and 5 particles reached steady state before 30 000 viscous time units. At $Re_\tau = 1000$ however, a longer time (approximately 40 000 in wall units) was required for the distribution to reach steady state for the more inertial ($\tau_p^+ = 30$) particles. To our knowledge, this is the first time that such long simulations are realized to study the dynamics of prolate ellipsoids, at different values of the Reynolds number, in a turbulent channel flow.

4. Preferential concentration

In a turbulent flow near solid boundaries, the spatial organization of the coherent vortices (Robinson 1991) induces a characteristic preferential concentration of inertial particles. Particularly, Kaftori, Hetsroni & Banerjee (1995) showed that spherical, inertial particles accumulate in regions of negative streamwise fluid velocity fluctuation (the so-called low-speed streaks). Using DNS, this characteristic concentration was similarly observed for ellipsoidal particles by Zhang *et al.* (2001) and Mortensen *et al.* (2008*a*), with a small influence of λ. To illustrate this particle segregation, an instantaneous visualization of the fluctuation field, $u_x'^+$, as well as ellipsoids located in $1 < y_p^+ < 5$ are presented in figure 1. It should be noted that this phenomenon could be emphasized using other techniques. Some of them were recently applied to experimental and DNS data for spherical particles (see, for instance, Fong, Amili & Coletti 2019; Jie *et al.* 2022). Results are given for $\lambda = 3$ only because the influence of the aspect ratio is minor. From figure 1(*a*,*b*), small differences are visible between $\tau_p^+ = 5$ and 30 ellipsoids at $Re_\tau = 180$. In both cases, particle distribution is not random, and long particle streaks can be observed. There is a good agreement between the particle streaks and regions where the fluctuations of the streamwise velocity component are negative, corresponding to low-speed fluid streaks. More $\tau_p^+ = 30$ particles nonetheless appear to be located in regions of positive $u_x'^+$.

Figure 1(*c*,*d*) presents a similar visualization for the case $Re_\tau = 1000$. While the general appearance of the instantaneous flow seems more complex, due to the smaller size of the turbulent flow structures, a careful examination reveals that the main features observed at $Re_\tau = 180$ are still visible. Long particle streaks can be observed, and these correspond to regions of negative $u_x'^+$. This qualitative independence of the preferential concentration to the Reynolds number was also observed by Bernardini (2014) for spherical particles. In addition, Bernardini noted that the spacing between the streaks remains constant, in wall units ($\delta_z^+ \approx 120$), as the Reynolds number increases. This is similarly observed for the ellipsoids, and suggests that the universal organisation of inertial particles in the viscous sublayer does not depend on their shape.

To highlight the preferential sampling of the flow by the particles, the probability density function (p.d.f.) of the fluctuation of the streamwise component of the fluid translational velocity conditioned at particle location, $\tilde{u}_x'^+$, is presented in figure 2. This statistic was also selected by Marchioli & Soldati (2002) to quantify the preferential concentration of inertial spheres in a turbulent channel flow at $Re_\tau = 150$ and by Yuan *et al.* (2018) for

https://doi.org/10.1017/jfm.2023.420 Published online by Cambridge University Press

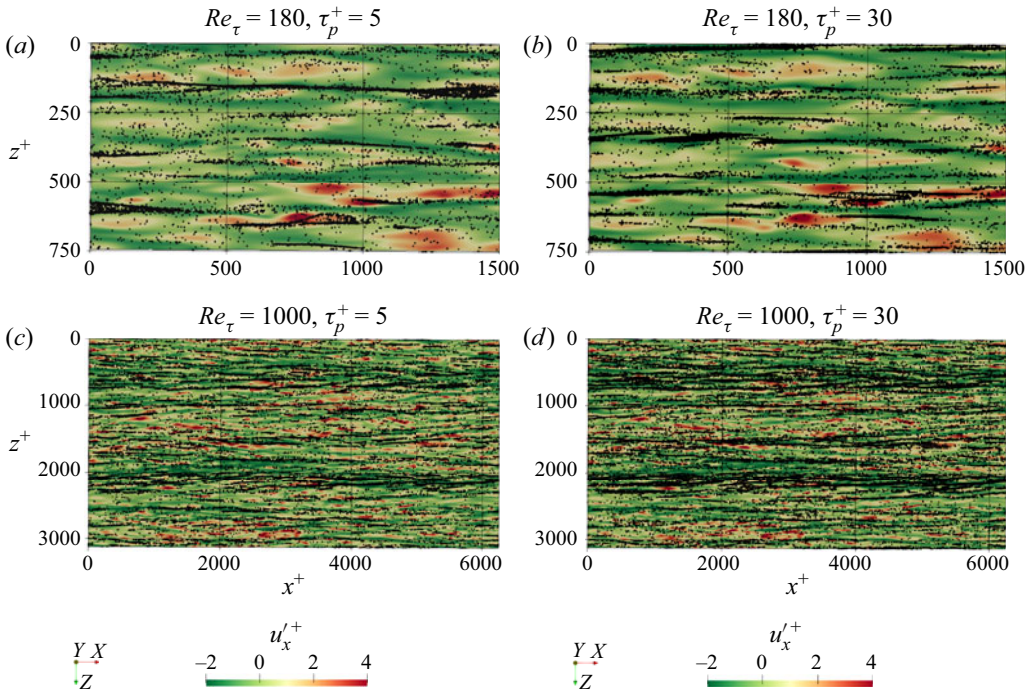

Figure 1. Visualization of the fluctuation of the streamwise component of the fluid translational velocity ($u_x'^+$) in the (x, z) plane at position $y^+ = 3$. The colouration represents the value of the fluctuations. The black dots represent the position of the centre of mass of $\lambda = 3$ ellipsoids with position $1 < y_p^+ < 5$. Results are shown for (*a*,*c*) $\tau_p^+ = 5$, (*b*,*d*) $\tau_p^+ = 30$, (*a*,*b*) $Re_\tau = 180$, (*c*,*d*) $Re_\tau = 1000$.

inertial ellipsoids at $Re_\tau = 180$. To evaluate this quantity, the DNS fluid velocity field is first interpolated at the particle location using the method mentioned in § 3. Statistics are then extracted by averaging over time and over the particles located in the slab $4 < y^+ < 5$. The p.d.f. of $u_x'^+$, the fluctuation of the streamwise component of the unconditioned fluid velocity is also presented. The peak of the p.d.f., both for $\tilde{u}_x'^+$ and $u_x'^+$, is visible for negative streamwise fluctuations, and it is higher for the fluid seen by the particles than for the unconditioned fluid. This corresponds to the characteristic particles accumulation in low-speed fluid streaks, which was observed in figure 1. The positive skew of the p.d.f. of $u_x'^+$ nonetheless indicates the rare occurrence of strong events associated to positive streamwise velocity fluctuations. The p.d.f. of the velocity fluctuations of the fluid seen by the particles exhibits a weaker skew, and the more intense events experienced by the particles depend on their relaxation time. For instance, the tail of the p.d.f. for $\tau_p^+ = 30$ particles (figure 2*b*) is longer than for $\tau_p^+ = 5$ (figure 2*a*), indicating a higher probability to experience strong positive streamwise velocity fluctuations. This trend reflects the different characteristics of the regions of the flow preferentially sampled by particles with respect to their relaxation time. Increasing the flow Reynolds number does not significantly alter the general shape of the p.d.f., but a higher probability of strong positive velocity fluctuation events can be noticed at higher Re_τ, both for the fluid and for the fluid seen by the particles.

To more finely quantify the influence of the flow Reynolds number on preferential concentration, we analyse how the fluctuations of the fluid seen by the particles are distributed in terms of the four types of turbulent events contributing to Reynolds

https://doi.org/10.1017/jfm.2023.420 Published online by Cambridge University Press

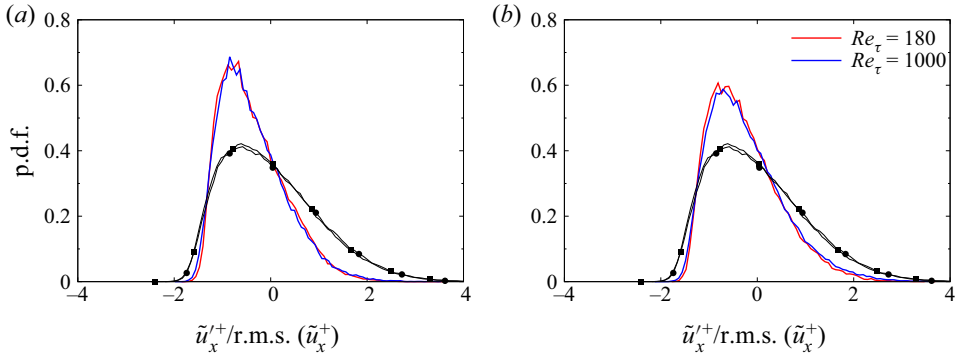

Figure 2. Probability density function (p.d.f.) of the fluctuation of the streamwise component of the fluid translational velocity sampled by the particles in the region $4 < y^+ < 5$. Results are shown for (*a*) $\tau_p^+ = 5$, (*b*) $\tau_p^+ = 30$. Black line with symbols: unconditioned fluid. Circles: $Re_\tau = 180$; squares: $Re_\tau = 1000$. The data are normalized by the velocity r.m.s.

	$4 < y^+ < 5$				$28 < y^+ < 32$				Channel core			
	Q_1	Q_2	Q_3	Q_4	Q_1	Q_2	Q_3	Q_4	Q_1	Q_2	Q_3	Q_4
$\tau_p^+ = 1, Re_\tau = 180$	12.5	35.5	22.9	29.1	17.3	33.7	14.4	34.6	26.5	22.8	22.3	28.4
$\tau_p^+ = 1, Re_\tau = 1000$	12.4	36.5	24.1	27.0	16.9	34.6	17.3	31.2	26.5	22.8	21.8	28.9
$\tau_p^+ = 5, Re_\tau = 180$	8.90	44.4	27.3	19.4	14.1	39.0	15.5	31.4	28.3	21.0	20.3	30.4
$\tau_p^+ = 5, Re_\tau = 1000$	8.50	44.5	29.0	18.0	14.6	39.1	18.2	28.1	26.8	22.7	22.4	28.1
$\tau_p^+ = 30, Re_\tau = 180$	10.3	40.3	26.3	23.1	17.4	37.4	15.2	30.0	29.9	19.3	18.8	32.0
$\tau_p^+ = 30, Re_\tau = 1000$	10.9	38.9	27.0	23.2	16.7	38.5	18.5	26.3	28.7	21.0	20.8	29.5

Table 3. Quadrant analysis of the fluid seen by the particles for $\lambda = 3$ ellipsoids at different wall-normal locations in the channel. The channel core is defined as $170 < y^+ < 180$ and $950 < y^+ < 1000$ for $Re_\tau = 180$ and 1000, respectively.

shear stress. These are called the quadrants and are characterized by the sign of u_x' and u_y' (Wallace, Eckelmann & Brodkey 1972). The first quadrant (Q_1), $u_x' > 0$ and $u_y' > 0$, corresponds to the motion of a fluid parcel with high streamwise velocity towards the channel centre; the second quadrant (Q_2), $u_x' < 0$ and $u_y' > 0$, is associated to ejections of low-speed fluid towards the channel core; the third quadrant (Q_3), $u_x' < 0$ and $u_y' < 0$, corresponds to the motion of low-speed fluid towards the wall; the fourth quadrant (Q_4), $u_x' > 0$ and $u_y' < 0$, is representative of the motion of high speed fluid towards the wall (sweeps). From such an analysis, Marchioli & Soldati (2002) showed that Q_2 and Q_4 events are strongly correlated to spherical particle motion toward and outward from the wall.

The average percentage of particles in each quadrant at different wall-normal locations in the channel is presented in table 3 for three values of the relaxation time. Only the results for $\lambda = 3$ are reported, because from a quantitative perspective, we did not notice important differences with the other aspect ratios. In the viscous sublayer ($4 < y^+ < 5$), at $Re_\tau = 180$, most of $\tau_p^+ = 5$ and 30 ellipsoids (65–70 %) sample Q_2 and Q_3 events, which correspond to regions where $u_x' < 0$. This result is connected with the accumulation of

https://doi.org/10.1017/jfm.2023.420 Published online by Cambridge University Press

$\tau_p^+ = 5$ and 30 particles in the low-speed streaks that was observed in figure 1(*a*,*b*). The picture is different for $\tau_p^+ = 1$ ellipsoids, which preferentially sample Q_2 and Q_4 events. At a further distance from the wall, particles interact differently with the turbulent flow, and sample different regions. Results from the quadrant analysis at $y^+ \approx 30$ are presented in table 3. In this region, a large fraction of the ellipsoids are surrounded by Q_2 and Q_4 events. This compares well with what Vinkovic *et al.* (2011) observed for $\tau_p^+ = 5$ spherical particles in a channel at $Re_\tau = 587$ around $y^+ = 38$. Note that the results presented in table 3 show that such events are also dominant for $\tau_p^+ = 1$ and 30 in this region. Finally, in the channel core, ellipsoids preferentially sample Q_1 and Q_4 events. These correspond to regions where the fluctuations of the streamwise velocity are of a positive sign, and contrast with the preferential concentration in the near-wall and buffer regions. It is noteworthy to mention that the distribution of the fluctuations of the fluid velocity sampled at particle location is not isotropic in the channel core. This result compares well to the anisotropy of the fluid velocity distribution in the channel core reported by Kim, Moin & Moser (1987) at $Re_\tau = 180$.

The results presented in table 3 also show the influence of the Reynolds number on the properties of the fluid velocity seen by the particles. Increasing the value of Re_τ does not deeply alter the distribution of the fluctuations of the velocity of the fluid seen by the particles. A finer comparison nonetheless reveals a complex evolution of the quadrant distribution, with different trends depending on the position in the channel and on the relaxation time. In the near-wall region the influence of Re_τ on the turbulent events surrounding the particles depends on the relaxation time. For example, $\tau_p^+ = 1$ ellipsoids experience more Q_2 (ejection) events at higher values of Re_τ, while the probability of encountering such events decreases for $\tau_p^+ = 30$. Higher values of Re_τ are also associated with a decrease of the fraction of Q_4 (sweep) events sampled by $\tau_p^+ = 1$ ellipsoids in this region, but this is not the case for $\tau_p^+ = 30$. In the buffer layer results presented in table 3 show that the influence of Re_τ on the quadrants is similar for all relaxation times. The fraction of Q_4 events decreases, while that of Q_3 increases. Ellipsoids surrounded by fluid moving towards the wall therefore experience more negative streamwise velocity fluctuations at higher values of Re_τ. Finally, in the channel core there is a weak influence of Re_τ on the turbulent events experienced by $\tau_p^+ = 1$ ellipsoids. For more inertial particles, however, a clear increase of the fraction of Q_2 and Q_3 events can be noticed, while the probability of Q_1 and Q_4 events decreases. This indicates that $\tau_p^+ = 5$ and 30 ellipsoids are more likely to be surrounded by negative streamwise velocity fluctuations in the channel core at higher Re_τ. This evolution is likely related to the interaction of these particles with very-large-scale motions (VLSM), which have a more important contribution to the turbulent flow dynamics as Re_τ increases (Balakumar & Adrian 2007). It was previously shown that these large-scale structures have a strong effect on the preferential concentration of spherical particles with a relaxation time ranging between $5 < \tau_p^+ < 300$ (Jie *et al.* 2022). This result seems to apply to ellipsoidal particles as well. Increasing the flow Reynolds number results in a more homogeneous distribution of the velocity fluctuations of the fluid seen by $\tau_p^+ = 5$ and 30 particles in this region.

These observations show that increasing the flow Reynolds number has an effect on the fluid velocity fluctuations sampled by the particles, especially in the buffer region, and in the channel core for moderately inertial particles. To better understand the influence of Re_τ on the particle dynamics, several statistics describing the particle and fluid translational velocity seen by the particles are analysed in the next section.

https://doi.org/10.1017/jfm.2023.420 Published online by Cambridge University Press

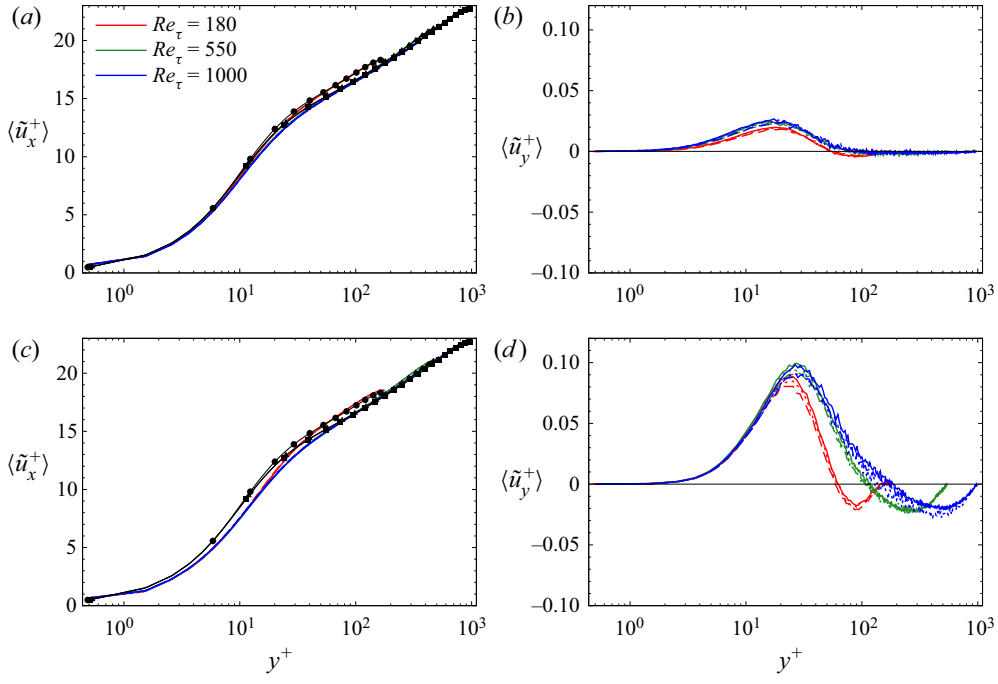

Figure 3. Average value of the streamwise (a,c) and wall-normal (b,d) components of the translational velocity of the fluid at particle position, as a function of y^+. Continuous line, $\lambda = 1$; dotted line, $\lambda = 3$; dashed line, $\lambda = 10$. Results are shown for (a,b) $\tau_p^+ = 1$, (c,d) $\tau_p^+ = 30$. Black line with symbols: unconditioned fluid. Circles: $Re_\tau = 180$; triangles: $Re_\tau = 550$; squares: $Re_\tau = 1000$.

5. Translational velocity statistics

5.1. *Mean fluid seen velocity and drift velocity*

We now describe the statistical properties of the fluid velocity conditioned at particle location (also referred to as fluid velocity seen or sampled by the particles in the following). As previously explained, the DNS fluid velocity field is first interpolated at the particle location using the method mentioned in § 3 to evaluate this quantity. Statistics are then extracted by averaging over time and over the particles located in a given wall-normal slab whose thickness is provided by the Eulerian mesh. The average streamwise component of the fluid velocity seen by the particles is presented in figure 3(a,c) for relaxation times $\tau_p^+ = 1$ and 30, and for three aspect ratios. At $Re_\tau = 180$, Mortensen *et al.* (2008*b*) did not notice a strong influence of λ on this statistic, and this result was later confirmed by the experimental measurements of Abbasi Hoseini *et al.* (2015). This statement remains valid at $Re_\tau = 550$ and 1000. In addition, the evolution of the streamwise component of the fluid velocity seen by the particles with Re_τ is analogous to that of the unconditioned fluid. In the viscous sublayer the average velocity, expressed in wall units, is independent of the Reynolds number, but the maximum value of $\langle \tilde{u}_x^+ \rangle$ increases in the channel core. These observations are valid for all the relaxation times considered.

The mean wall-normal component of the fluid velocity seen by the particles is presented in figure 3(b,d). The average $\tilde{u}_y^+$ is not zero, because of the preferential particle segregation in the flow field. Increasing Re_τ has a notable influence on this statistic, which depends on the position in the channel and relaxation time. For $\tau_p^+ = 1$, the mean wall-normal velocity of the fluid seen by the particles increases with Re_τ, everywhere in the channel. This can

https://doi.org/10.1017/jfm.2023.420 Published online by Cambridge University Press

be noticed in the buffer region, where $\langle \tilde{u}_y^+ \rangle$ is maximum. It is interesting to observe that this result cannot be explained by the evolution of the quadrant distribution. For example, at $y^+ = 30$, results presented in table 3 indicate that 51 % of the $\tau_p^+ = 1$ particles sample regions of positive $\tilde{u}_y'^+$ at $Re_\tau = 180$ (the sum of Q_1 and Q_2). This fraction is 51.5 % at $Re_\tau = 1000$, and should not result in a visible increase of $\langle \tilde{u}_y^+ \rangle$. Therefore, the increase of $\langle \tilde{u}_y^+ \rangle$ with Re_τ observed in figure 3(*b*) is caused by the higher intensity of the fluctuations of the fluid seen by the particles. In the channel core, for $\tau_p^+ = 1$, $\langle \tilde{u}_y^+ \rangle$ is slightly negative at $Re_\tau = 180$, and does not significantly vary with the Reynolds number.

For $\tau_p^+ = 30$, figure 3(*d*) also shows that $\langle \tilde{u}_y^+ \rangle$ increases with Re_τ in the buffer region. Around $y^+ = 30$, the maximum of $\langle \tilde{u}_y^+ \rangle$ is higher for $Re_\tau = 550$ and 1000 than for $Re_\tau = 180$. This is coherent with the increase of the number of events associated with positive $\tilde{u}_y'$ sampled by the particles at higher Re_τ (table 3). In the near-wall region and in the channel core, the average wall-normal velocity of the fluid seen by the particles does not vary with Re_τ. This result was not expected from the results presented in table 3, because the quadrant analysis at $y^+ = 5$ indicates that the fraction of $\tau_p^+ = 30$ particles sampling Q_1 and Q_2 events is lower if the value of Re_τ is higher (50.6 % at $Re_\tau = 180$ and 49.8 % at $Re_\tau = 1000$). The expected outcome would be a lower value of $\langle \tilde{u}_y^+ \rangle$ for higher Re_τ. The fact that the mean value of the wall-normal velocity seen by the particles does not decrease indicates that the intensity of the turbulent events sampled by the particles increases with Re_τ. Finally, in the near-wall region and in the channel core, $\langle \tilde{u}_y^+ \rangle$ is mostly unaffected by the value of Re_τ.

To obtain more information about the properties of the fluid sampled by the particles, the streamwise component of the translational drift velocity is presented in figure 4. The translational drift velocity corresponds to the average fluctuation of the velocity of the fluid sampled by the particles, computed by taking the unconditioned fluid velocity average as a reference,

$$u_{dx} = \langle \tilde{u}_x - \langle u_x \rangle \rangle. \tag{5.1}$$

In the channel at $Re_\tau = 180$, negative values of u_{dx}^+ up to $y^+ \approx 50$ indicate that the particles sample regions of the flow where the streamwise velocity is lower than the average, that is, where the fluctuations of the streamwise velocity are negative. This observation is connected with the results presented in table 3: regardless of the relaxation time and aspect ratio, a majority of particles sample Q_2 and Q_3 events. Increasing the flow Reynolds number has a notable influence on u_{dx}^+, which is similar for all aspect ratios but differs as a function of the relaxation time.

For $\tau_p^+ = 1$ (figure 4*a*), the region of the channel for which u_{dx}^+ is negative increases with Re_τ. In addition, a decrease of the drift velocity is observed in this region, indicating that ellipsoids see more negative fluctuations of the streamwise fluid velocity as the Reynolds number increases. This is connected with the results presented in table 3 at $y^+ = 5$ and 30. There is a higher fraction of particles in Q_2 and Q_3 events at $Re_\tau = 1000$ than at $Re_\tau = 180$ at these two locations. Similar observations can be made for $\tau_p^+ = 5$ (figure 4*b*), although the influence of increasing from $Re_\tau = 550$ to $Re_\tau = 1000$ is less important for this relaxation time. A notable exception is for $\lambda = 10$. For this aspect ratio, increasing the Reynolds number from $Re_\tau = 550$ to $Re_\tau = 1000$ results in a significant increase of the fraction of the channel where the drift velocity is negative for $\tau_p^+ = 5$. In consequence, the sign of the drift velocity differs from that observed for $\lambda = 1$ and 3 over a large fraction of the channel height. This result is remarkable because such influence of the aspect ratio is not visible at $Re_\tau = 180$ and 550. Therefore, there might be unexpected effects of the aspect ratio on the particle statistics at higher values of the Reynolds number.

https://doi.org/10.1017/jfm.2023.420 Published online by Cambridge University Press

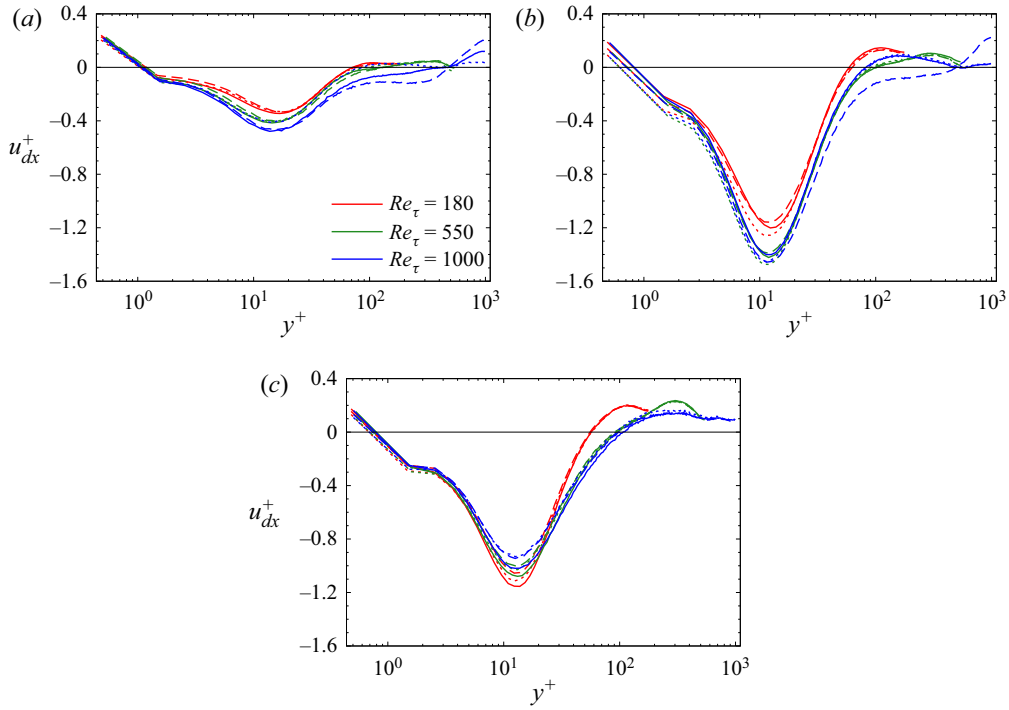

Figure 4. Streamwise component of the translational drift velocity as a function of y^+. Continuous line, $\lambda = 1$; dotted line, $\lambda = 3$; dashed line, $\lambda = 10$. Results are shown for (*a*) $\tau_p^+ = 1$, (*b*) $\tau_p^+ = 5$, (*c*) $\tau_p^+ = 30$.

Such dependence of the drift velocity to the flow Reynolds number is likely due to the interaction of the ellipsoidal particles with the VLSM present in the flow at $Re_\tau = 1000$. For instance, Wang & Richter (2019) reported that the VLSM have a strong influence on the streamwise drift velocity of inertial spherical particles in the outer region of an open channel flow. The present results suggest that the influence of the VLSM on the drift velocity additionally depends on the particle shape, especially for weak and moderate particle inertia. For $\tau_p^+ = 30$, such influence of the aspect ratio is not visible in figure 4(*c*). There is however a different evolution of u_{dx}^+ with the Reynolds number. The minimum value of the drift velocity increases with Re_τ for $\tau_p^+ = 30$, indicating a decrease of the preferential concentration of such particles in regions of negative streamwise fluid velocity fluctuations. This trend is the opposite of what was observed for smaller relaxation times. Finally, increasing the flow Reynolds number has a weak effect on u_{dx}^+ in the channel core and only results in a slight decrease of the drift velocity in this region.

5.2. *Fluctuations of the particle and fluid seen velocities*

We now examine the influence of Re_τ on the r.m.s. of the fluid seen and particle translational velocities. The r.m.s. of the streamwise component of the velocity of the fluid at particle position is presented in figure 5 for relaxation times $\tau_p^+ = 5$ (figure 5*a*) and 30 (figure 5*c*). In a general manner, there is a similar evolution of r.m.s.(u_x^+) and r.m.s.($\tilde{u}_x^+$): increasing the Reynolds number leads to higher velocity fluctuations, everywhere in the channel. A well-known effect of particle inertia observed both for spheres and ellipsoids (Mortensen *et al.* 2008*a*) at $Re_\tau = 180$ is that the r.m.s. of the fluid seen by the particles

https://doi.org/10.1017/jfm.2023.420 Published online by Cambridge University Press

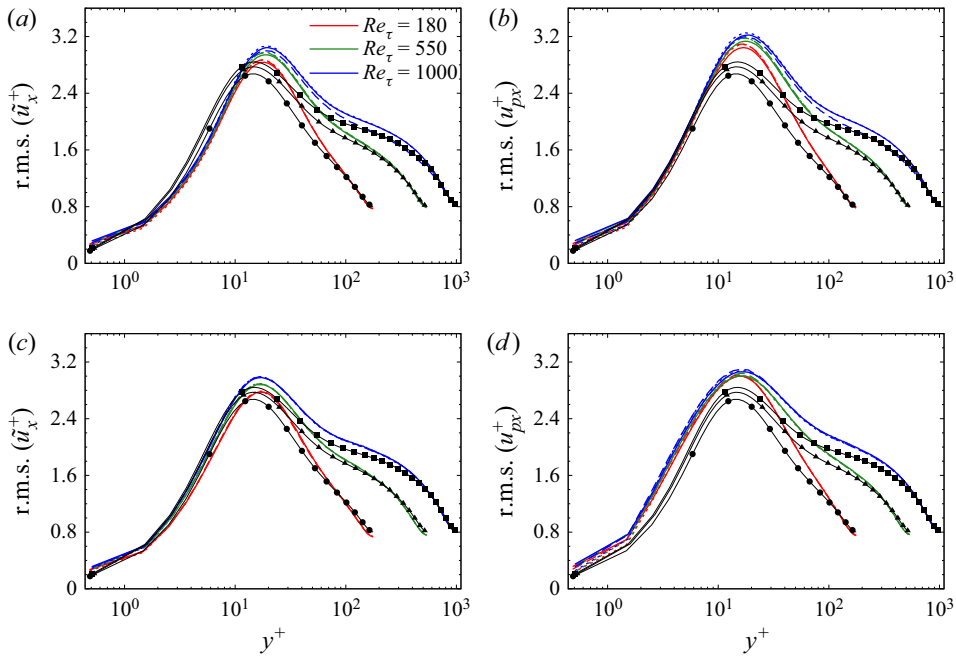

Figure 5. The r.m.s. of the streamwise component of the fluid translational velocity at particle position (*a*,*c*) and of the particle translational velocity (*b*,*d*) as a function of y^+. Continuous line, $\lambda = 1$; dotted line, $\lambda = 3$; dashed line, $\lambda = 10$. Results are shown for (*a*,*b*) $\tau_p^+ = 5$, (*c*,*d*) $\tau_p^+ = 30$. Black line with symbols: unconditioned fluid velocity. Circles: $Re_\tau = 180$; triangles: $Re_\tau = 550$; squares: $Re_\tau = 1000$.

is higher than r.m.s.(u_x^+). Figure 5(*a*,*c*) shows that this observation does not depend on the Reynolds number, and neither does the position at which r.m.s.$(\tilde{u}_x^+)$ becomes higher than r.m.s.(u_x^+). In figure 5(*a*) we can nonetheless observe that for $\tau_p^+ = 5$, r.m.s.$(\tilde{u}_x^+)$ does not depend on λ for $Re_\tau = 180$ and 550, but this is not the case for $Re_\tau = 1000$. In the channel core the r.m.s. of the fluid seen by $\lambda = 10$ and $\tau_p^+ = 5$ ellipsoids is nearly equal to that of the fluid for this Reynolds number. For $\tau_p^+ = 30$, these results weakly depend on the aspect ratio, up to $Re_\tau = 1000$.

These results can be compared with the particle velocity r.m.s., which are presented in figure 5(*b*,*d*). In their study, Mortensen *et al.* (2008*a*) showed that r.m.s.(u_{px}^+) for ellipsoidal particles at $Re_\tau = 180$ is greater than that of the fluid, everywhere in the channel. This is a well-known effect induced by the presence of a mean fluid velocity gradient, which was previously documented for spheres (see, for instance, Liljegren 1993). The present results confirm this trend for higher values of the Reynolds number. Previously, we also remarked that r.m.s.$(\tilde{u}_x^+)$ increases in a way similar to that of the fluid. This is the case for r.m.s.(u_{px}^+) as well. Nonetheless for $\tau_p^+ = 30$ (figure 5*d*), we remark that the increase of r.m.s.(u_{px}^+) is less pronounced than the increase observed for the fluid. To conclude, regardless of the Reynolds number, the effect of the aspect ratio on r.m.s.(u_{px}^+) is similar to that observed on r.m.s.$(\tilde{u}_x^+)$. There is generally a weak effect of this parameter, except for the r.m.s. for $\lambda = 10$ and $\tau_p^+ = 5$ in the central region of the channel at $Re_\tau = 1000$.

The wall-normal and spanwise components of the r.m.s. of the fluid translational velocity sampled at particle position are presented in figure 6(*a*,*c*) for $\tau_p^+ = 5$. For all three Reynolds numbers considered, r.m.s.$(\tilde{u}_y^+)$ and r.m.s.$(\tilde{u}_z^+)$ are lower than those of the fluid.

https://doi.org/10.1017/jfm.2023.420 Published online by Cambridge University Press

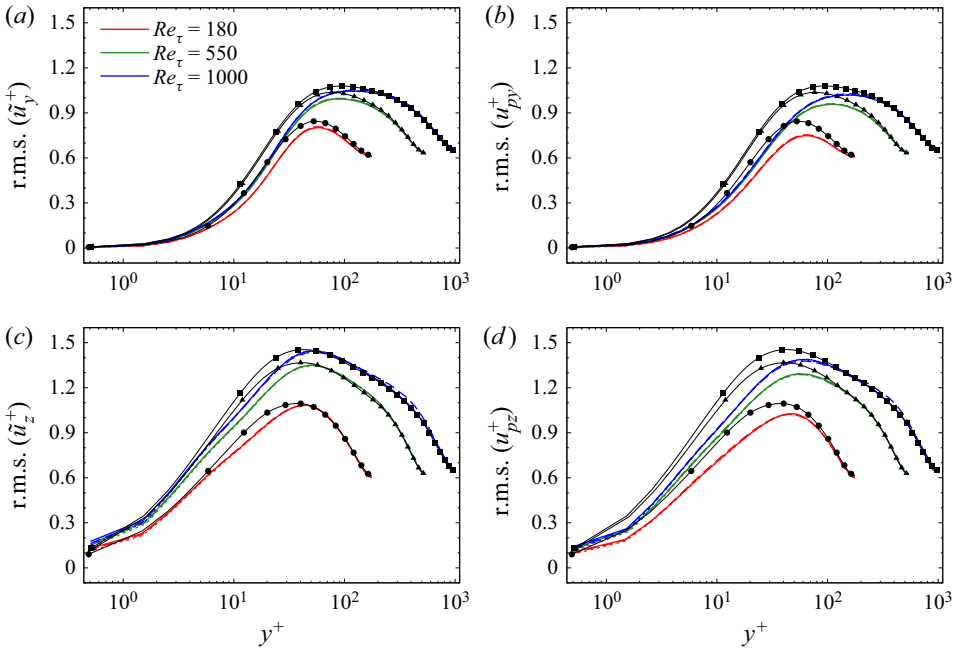

Figure 6. The r.m.s. of the fluid translational velocity at particle position (*a*,*c*) and of the particle translational velocity (*b*,*d*) as a function of y^+ for particles with relaxation time $\tau_p^+ = 5$. Continuous line, $\lambda = 1$; dotted line, $\lambda = 3$; dashed line, $\lambda = 10$. Results are shown for (*a*,*b*) wall-normal component; (*c*,*d*) spanwise component. Black line with symbols: unconditioned fluid. Circles: $Re_\tau = 180$; triangles: $Re_\tau = 550$; squares: $Re_\tau = 1000$.

The influence of the aspect ratio on these components of r.m.s.$(\tilde{u}_i^+)$ is minor at $Re_\tau = 180$, and this statement remains true at $Re_\tau = 550$ and 1000 as well. Figure 6(*b*,*d*) indicates that the same conclusions apply to the r.m.s. of the wall-normal and spanwise components of the particle translational velocity. Results for $\tau_p^+ = 1$ and $\tau_p^+ = 30$ similarly reveal a weak influence of λ for all the Reynolds numbers considered and are not presented for brevity reasons.

6. Angular velocity statistics

6.1. *Mean particle and fluid seen angular velocities*

To complete this study, we now examine the influence of Re_τ on the angular velocity statistics.

The mean angular velocity of the fluid seen by the particles is presented in figure 7(*a*,*c*) for $\tau_p^+ = 1$ and 30. The angular velocity of the fluid sampled by the particles is nearly the same as that of the fluid, regardless of the aspect ratio, relaxation time and Reynolds number. Nonetheless, in the viscous sublayer the mean angular velocity of the fluid seen by the particles is slightly lower than the average angular velocity of the fluid, while it is slightly higher around $y^+ = 30$. These differences are more important for $\tau_p^+ = 30$ than for $\tau_p^+ = 1$. Because the average angular velocity of the fluid seen by the particles only depends on the wall-normal derivative of $\langle \tilde{u}_x^+ \rangle$, it can be related to the preferential concentration. In the viscous sublayer the particles are located in low-speed streaks (table 3), corresponding to regions where $\langle \tilde{u}_x^+ \rangle < \langle u_x^+ \rangle$. The wall-normal derivative of the

https://doi.org/10.1017/jfm.2023.420 Published online by Cambridge University Press

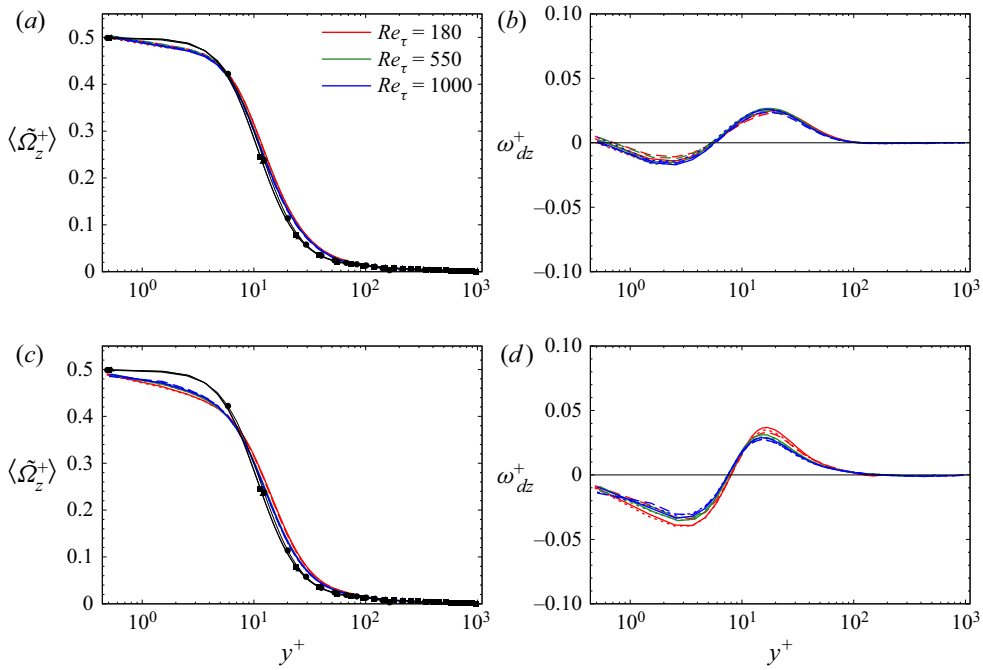

Figure 7. Average spanwise component of the angular velocity of the fluid at particle position (*a*,*c*) and angular drift velocity (*b*,*d*) as a function of y^+. Continuous line, $\lambda = 1$; dotted line, $\lambda = 3$; dashed line, $\lambda = 10$. Results are shown for (*a*,*b*) $\tau_p^+ = 1$, (*c*,*d*) $\tau_p^+ = 30$. Black line with symbols: unconditioned fluid. Circles: $Re_\tau = 180$; triangles: $Re_\tau = 550$; squares: $Re_\tau = 1000$.

mean streamwise translational velocity of the fluid seen by the particles in this region is therefore lower than the one of the fluid. This explains the lower values of $\langle \tilde{\Omega}_z^+ \rangle$ observed in figure 7(*a*,*c*) up to $y^+ = 8$. In the buffer region, figure 3(*a*,*c*) shows that $\langle \tilde{u}_x^+ \rangle$ increases more quickly than $\langle u_x^+ \rangle$. This is consistent with the values of $\langle \tilde{\Omega}_z^+ \rangle$ being higher than $\langle \Omega_z^+ \rangle$. Increasing the value of the Reynolds number does not strongly modify the mean angular velocity of the fluid, nor the mean angular velocity of the fluid sampled by the particles.

In order to highlight the differences between the angular velocity of the fluid seen by the particles and the mean fluid angular velocity, figure 7(*b*,*d*) presents the angular drift velocity, the average fluctuation of the angular velocity of the fluid conditioned at particle position, computed with the average fluid angular velocity as a reference,

$$\omega_{dz} = \langle \tilde{\Omega}_z - \langle \Omega_z \rangle \rangle. \tag{6.1}$$

For the two relaxation times considered, the angular drift velocity is negative in the viscous sublayer and positive in the buffer region. This is consistent with the observation previously reported from figure 7(*a*,*c*). In figure 7(*b*) we remark that increasing the flow Reynolds number has a minor effect on the angular drift velocity for $\tau_p^+ = 1$ particles. For $\tau_p^+ = 30$ (figure 7*d*), the magnitude of ω_{dz}^+ is lower for higher values of Re_τ. On average, at higher Re_τ, the angular velocity of the fluid seen by the particles is closer to that of the unconditioned fluid. Finally, the influence of the aspect ratio on the angular drift velocity is marginal, which confirms the previous remarks about the angular velocity of the fluid seen by the particles.

https://doi.org/10.1017/jfm.2023.420 Published online by Cambridge University Press

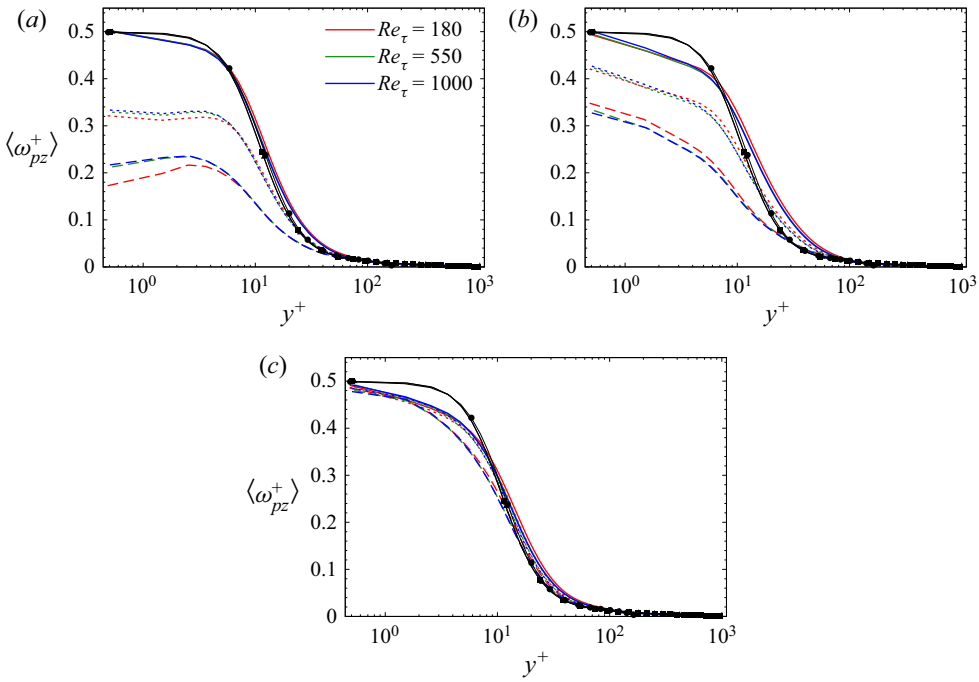

Figure 8. Average spanwise component of the particle angular velocity as a function of y^+. Continuous line, $\lambda = 1$; dotted line, $\lambda = 3$; dashed line, $\lambda = 10$. Results are shown for (*a*) $\tau_p^+ = 1$, (*b*) $\tau_p^+ = 5$, (*c*) $\tau_p^+ = 30$. Black line with symbols: unconditioned fluid. Circles: $Re_\tau = 180$; triangles: $Re_\tau = 550$; squares: $Re_\tau = 1000$.

The ellipsoids mean angular velocity is presented in figure 8. In the near-wall region the particle mean angular velocity strongly depends on the aspect ratio and relaxation time. This is a consequence of the periodic rotation orbits caused by the mean velocity gradient in this region. The characteristics of the rotation orbits strongly vary with the particle shape and inertia (Lundell & Carlsson 2010; Zhao *et al.* 2015*b*). For example, $\lambda = 10$ and $\tau_p^+ = 1$ particles have long rotation periods in the plane (x, z), where they spend extended periods of time spinning with their major axis aligned with the mean flow (Michel & Arcen 2021*b*). These conclusions, drawn up to $Re_\tau = 550$, can be extrapolated up to $Re_\tau = 1000$. On average, it results in a low mean spanwise angular velocity for high aspect ratios (figure 8*a*). Ellipsoids of relaxation time $\tau_p^+ = 30$, however, rotate around one of their minor axis and with a nearly constant angular velocity in the velocity-gradient (x, y) plane (Michel & Arcen 2021*b*). Their average angular velocity is close to that of the spherical particles, and also close to the mean angular velocity of the fluid (figure 8*c*).

In the near-wall region there is a notable influence of the Reynolds number on the mean angular velocity of $\lambda = 10$ and $\tau_p^+ = 1$ ellipsoids. Figure 8(*a*) clearly shows the increase of the mean angular velocity of these particles with Re_τ. There is an analogous influence of Re_τ on the angular velocity of $\lambda = 3$ and $\tau_p^+ = 1$ ellipsoids, although less important. A possible explanation can be obtained by examining the influence of the Reynolds number on the rotation mode of the ellipsoids. In the near-wall region higher values of Re_τ increase the alignment of the particle major axis with the mean vorticity for $\tau_p^+ = 1$ (Michel & Arcen 2021*b*). This stronger alignment induces a higher average particle angular velocity. For $\tau_p^+ = 30$ ellipsoids, increasing Re_τ results in an increase of the mean angle between the particle major axis and the velocity-gradient plane (Michel & Arcen 2021*b*).

https://doi.org/10.1017/jfm.2023.420 Published online by Cambridge University Press

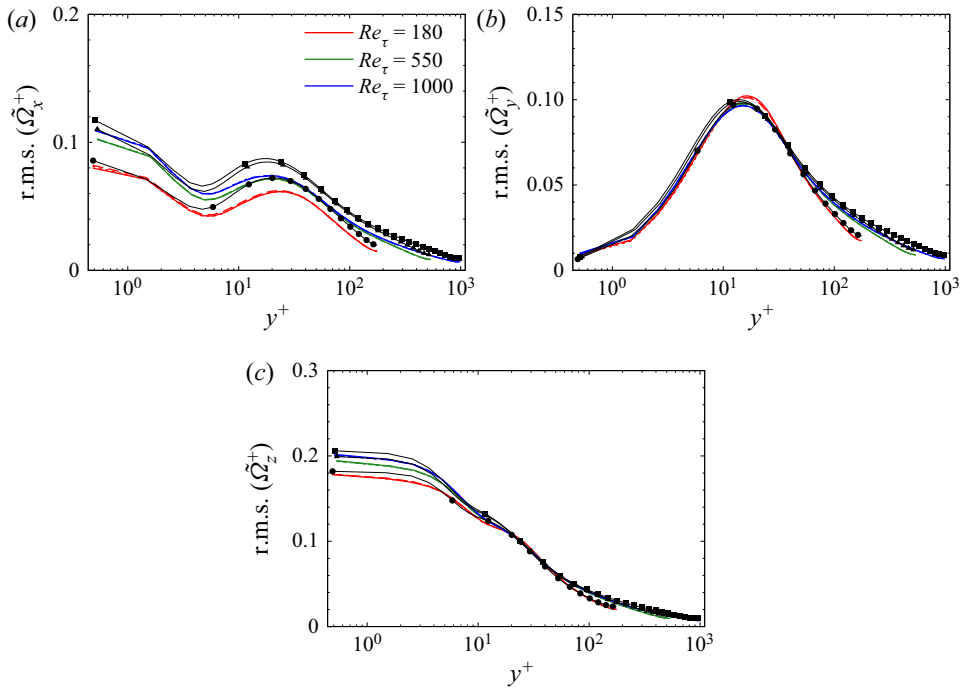

Figure 9. The r.m.s. of the streamwise (*a*), wall-normal (*b*) and spanwise (*c*) components of the angular velocity of the fluid at particle position as a function of y^+ for particles with relaxation time $\tau_p^+ = 30$. Continuous line, $\lambda = 1$; dotted line, $\lambda = 3$; dashed line, $\lambda = 10$. Black line with symbols: unconditioned fluid. Circles: $Re_\tau = 180$; triangles: $Re_\tau = 550$; squares: $Re_\tau = 1000$.

While a decrease of the mean angular velocity of these particles could be expected, figure 8(*c*) suggests only minor changes of $\langle \omega_{pz}^+ \rangle$ with the flow Reynolds number for such ellipsoids. In figure 8(*b*), however, we note a slight decrease of the mean angular velocity of $\lambda = 10$ and $\tau_p^+ = 5$ particles when Re_τ increases. These ellipsoids have a hybrid rotation mode, that share characteristics from both rotations of $\tau_p^+ = 1$ and $\tau_p^+ = 30$ ellipsoids. For moderate inertia, the modification of the rotation orbits when Re_τ increases therefore results in a reduction of the average angular velocity.

6.2. *Fluctuations of the particle and fluid seen angular velocities*

To conclude this study, we examine the effect of the flow Reynolds number on the fluctuations of the angular velocity. The r.m.s. of the three components of the angular velocity of the fluid sampled at particle position are presented in figure 9. Only the results for $\tau_p^+ = 30$ are presented because the influence of τ_p^+ on this statistic is minor. The intensity of r.m.s.$(\tilde{\Omega}_x^+)$ and r.m.s.$(\tilde{\Omega}_z^+)$ increases with the Reynolds number. This is clearly visible in the near-wall region and to a lesser extent in the buffer region. In contrast, r.m.s.$(\tilde{\Omega}_y^+)$ does not strongly vary with Re_τ. This trend is similar to that observed for the r.m.s. of the angular velocity of the unconditioned fluid (black line with symbols). Similarly to Mortensen *et al.* (2008*a*), a minor influence of the aspect ratio on the r.m.s.$(\tilde{\Omega}_i^+)$ at $Re_\tau = 180$ is noted. This weak effect of λ persists for higher values of Re_τ.

https://doi.org/10.1017/jfm.2023.420 Published online by Cambridge University Press

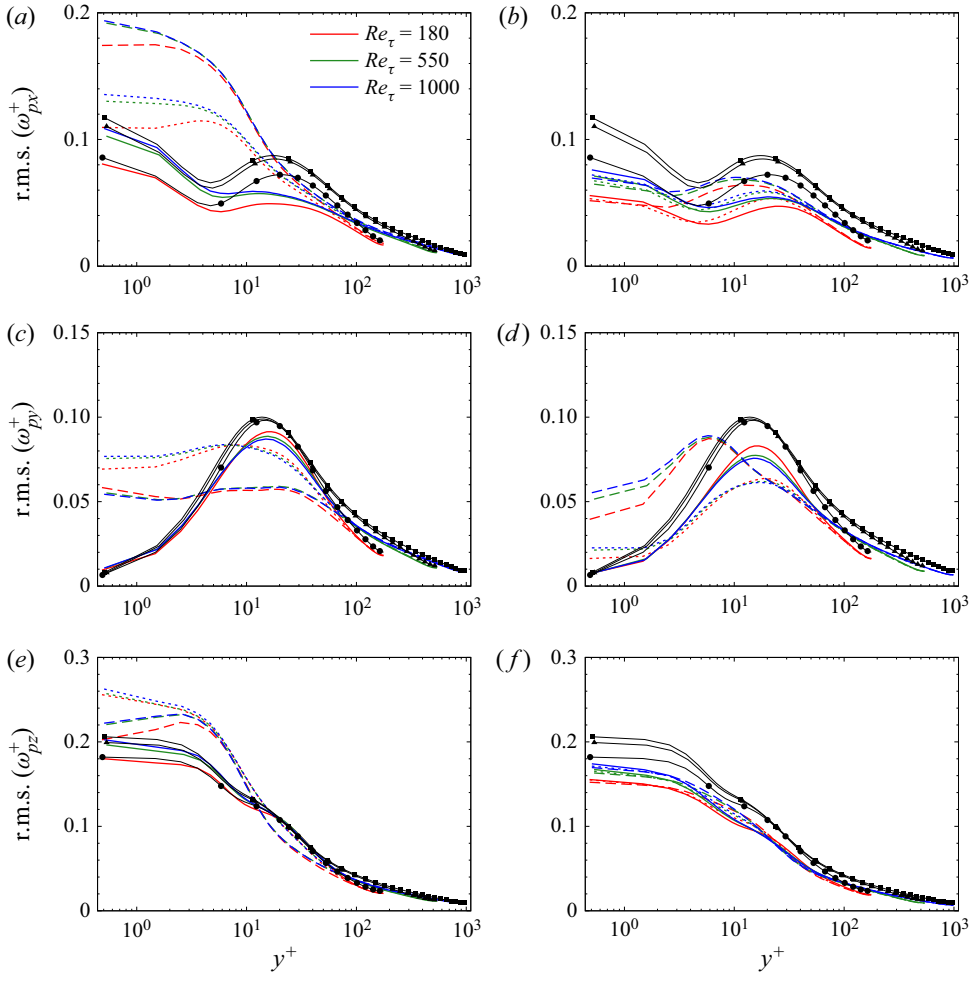

Figure 10. The r.m.s. of the streamwise (*a*,*b*), wall-normal (*c*,*d*) and spanwise (*e*,*f*) components of the particle angular velocity as a function of y^+. Continuous line, $\lambda = 1$; dotted line, $\lambda = 3$; dashed line, $\lambda = 10$. Results are shown for (*a*,*c*,*e*) $\tau_p^+ = 1$, (*b*,*d*,*f*) $\tau_p^+ = 30$. Black line with symbols: unconditioned fluid. Circles: $Re_\tau = 180$; triangles: $Re_\tau = 550$; squares: $Re_\tau = 1000$.

Figure 10 presents the three components of the r.m.s. of the particle angular velocity for $\tau_p^+ = 1$ and 30. These statistics strongly depend on the particle shape and relaxation time, and this is a direct consequence of the rotation induced by the mean velocity gradient. Spherical particles do not exhibit preferential rotation orbits and r.m.s.(ω_{pi}^+) are close to those of the fluid in the near-wall region for these particles. This trend is less pronounced for $\tau_p^+ = 30$ than for $\tau_p^+ = 1$ and this is a pure consequence of their higher inertia. For spherical particles, the intensity of r.m.s.(ω_{px}^+) and r.m.s.(ω_{pz}^+) increases with Re_τ. This is consistent with the evolution of the r.m.s. of the fluid angular velocity. The decrease of the maximum of r.m.s.(ω_{py}^+) for higher values of Re_τ is however unexpected. It matches neither the evolution of r.m.s.(Ω_y^+) nor the evolution of r.m.s.$(\tilde{\Omega}_y^+)$.

Concerning the ellipsoidal particles, it is known that they favour different rotation modes depending on their characteristics, which strongly influence the particle angular velocity r.m.s. All three components of the particle angular velocity r.m.s. exceed those of the fluid

https://doi.org/10.1017/jfm.2023.420 Published online by Cambridge University Press

in the near-wall region for $\tau_p^+ = 1$ ellipsoids, with a complex dependence of the angular velocity statistics to the aspect ratio. This is visible in figure 10(*a*) where r.m.s.(ω_{px}^+) are the highest for $\lambda = 10$ and in figure 10(*c*,*e*) where r.m.s.(ω_{py}^+) and r.m.s.(ω_{pz}^+) are maximum for $\lambda = 3$. The decrease of the intensity of the r.m.s. of the wall-normal component of the angular velocity with the particle length was also observed experimentally by Abbasi Hoseini *et al.* (2015) for weakly inertial fibres. The influence of the aspect ratio is less pronounced for $\tau_p^+ = 30$. Here r.m.s.(ω_{px}^+) and r.m.s.(ω_{pz}^+) follow the same evolution as r.m.s.(Ω_i), but have lower intensity. Only r.m.s.(ω_{py}^+) for $\lambda = 10$ strongly exceeds that of the fluid in the near-wall region. Everywhere in the channel, the main features characterizing the components of the ellipsoids angular velocity r.m.s. do not significantly vary between $Re_\tau = 180$ and $Re_\tau = 1000$. This effect was expected in the range $Re_\tau = 180$ to 550 since the ellipsoids rotation orbits only exhibit moderate variations (Michel & Arcen 2021*b*). The same trend is also noted from the analysis of the ellipsoids rotation orbits up to $Re_\tau = 1000$ (not shown here). Higher values of Re_τ nonetheless result in an increase of r.m.s.(ω_{px}^+) and r.m.s.(ω_{pz}^+), hence to a higher spread of the ellipsoids angular velocity. A finer analysis also reveals a complex evolution of r.m.s.(ω_{py}^+) with the Reynolds number. In figure 10(*c*), for example, the influence of Re_τ on the near-wall angular velocity r.m.s. for $\tau_p^+ = 1$ ellipsoids is more pronounced for $\lambda = 3$ than for $\lambda = 10$. This evolution is different from that of r.m.s.($\tilde{\Omega}_y^+$), and must therefore be associated to the influence of Re_τ on the ellipsoids rotation orbits. The effect of Re_τ on the rotation orbits of $\tau_p^+ = 1$ ellipsoids is more important for $\lambda = 3$ (Michel & Arcen 2021*b*), hence a more visible effect on the angular velocity r.m.s. of such particles. For $\tau_p^+ = 30$ ellipsoids (figure 10*d*), higher values of Re_τ result in a more important increase of r.m.s.(ω_{py}^+) for $\lambda = 10$ rather than for $\lambda = 3$. This is associated to the increase of the mean angle between the particle major axis and the velocity-gradient plane with the flow Reynolds number (Michel & Arcen 2021*b*). In general, it is difficult to predict the influence of Re_τ on the r.m.s.(ω_{py}^+) due to the strong nonlinearity of the coupling between the three components of the particle angular velocity (2.4*a*,*b*).

7. Conclusion

Direct numerical simulation coupled with a Lagrangian particle tracking has been used to investigate the effect of the flow Reynolds number effect on the dynamics of inertial, prolate ellipsoids in a turbulent channel flow. Three values of the aspect ratio $\lambda = 1, 3$ and 10 and three values of the relaxation time $\tau_p^+ = 1, 5$ and 30 have been examined for a total of nine particle sets. For each set, simulations have been performed at three values of the Reynolds number $Re_\tau = 180, 550$ and 1000, and conducted until the distribution of 300 000 particles has reached a statistically steady state.

First, the effect of the Reynolds number on the particle preferential concentration has been analysed by means of a quadrant analysis and visualizations. Increasing Re_τ does not significantly modify the preferential concentration. Nevertheless, a careful analysis reveals a slight evolution of the particle distribution in each quadrant everywhere in the channel. This effect depends on the particle relaxation time in the near-wall region ($y^+ < 5$) and in the channel core, suggesting a different response of the particles to the fluid fluctuations. A notable increase of the average wall-normal component of the translational velocity of the fluid seen by $\tau_p^+ = 30$ particles is noticed, and this effect cannot be explained by the evolution of the quadrant distribution. It is a consequence of the intensification of the fluctuations of the wall-normal component of the fluid translational velocity sampled by

https://doi.org/10.1017/jfm.2023.420 Published online by Cambridge University Press

the particles. Regardless of the particle shape and inertia, mean and r.m.s. properties of the translational velocity of the fluid seen by the particles evolve similarly to those of the fluid with Re_τ. Their intensity increases, moderately in the viscous sublayer but strongly in the buffer region and in the channel core. At low and moderate values of the Reynolds number, particle translation statistics weakly depend on the aspect ratio, and the influence of this parameter is only slightly more pronounced at $Re_\tau = 1000$. This result indicates that statistical properties about the translational velocity of ellipsoidal particles can be reasonably approximated by those of spherical particles up to $Re_\tau = 1000$.

Finally, we examined the effect of Re_τ on angular velocity statistics. Overall, the statistical properties of the angular velocity of the fluid seen by the particles have the same dependence to the flow Reynolds number than the fluid angular velocity. The average angular velocity and the r.m.s. of the wall-normal component weakly vary, while the r.m.s. of the streamwise and spanwise components increase with Re_τ. Higher values of the flow Reynolds number also result in stronger fluctuations of the streamwise and spanwise components of the particle angular velocity. The influence of Re_τ on the r.m.s. of the wall-normal component of the ellipsoids angular velocity and on the average particle angular velocity is more complex, because it depends on the evolution of their favoured rotation orbits. These orbits vary with the particle shape and inertia, and depend on the local value of the ratio between a turbulent time scale and the viscous time scale (Zhao *et al.* 2019). The stronger fluctuations of the turbulent shear at higher Re_τ noticeably affect the ellipsoids rotation statistics in the near-wall region. For example, the wall-normal component of the angular velocity r.m.s. for tumbling ellipsoids increases with Re_τ. This is associated to the increase of the mean angle between the particle major axis and the velocity-gradient plane with the flow Reynolds number. In the viscous sublayer, alignment of weakly inertial ellipsoids with the direction of the mean vorticity increases with Re_τ and this is associated to an increase of their average angular velocity. The derivation of a model reproducing the Reynolds number dependence of the angular velocity statistics of non-spherical particles represents a notable challenge when the Lagrangian particle tracking is coupled with a Reynolds-averaged Navier–Stokes (RANS) approach. This study provides a first look into the Reynolds number effects on the dynamics of non-spherical particles in a turbulent channel flow. Further investigation is nonetheless still required, both numerically and experimentally, to confirm the dependence of the dispersed phase statistics to Re_τ. Moreover, the fluid inertia contribution is neglected in the standard models of the hydrodynamic force and torque used in the present study. This shortcoming should be considered in the future using low-Reynolds-number approximations (Brenner 1961; Dabade, Marath & Subramanian 2015, 2016; Einarsson *et al.* 2015) and correlations derived at moderate Reynolds numbers from experiments and numerical simulations (Zastawny *et al.* 2012; Ouchene *et al.* 2016; Sanjeevi, Kuipers & Padding 2018; Fröhlich, Meinke & Schröder 2020).

Acknowledgements. High performance computing resources were partially provided by the EXPLOR centre hosted by the University de Lorraine.

Declaration of interests. The authors report no conflict of interest.

Author ORCIDs.
Antoine Michel https://orcid.org/0000-0001-8182-1131.

References

Abbasi Hoseini, A., Lundell, F. & Andersson, H.I. 2015 Finite-length effects on dynamical behavior of rod-like particles in wall-bounded turbulent flow. *Intl J. Multiphase Flow* **76**, 13–21.

https://doi.org/10.1017/jfm.2023.420 Published online by Cambridge University Press

ALIPOUR, M., PAOLI, M.D., GHAEMI, S. & SOLDATI, A. 2021 Long non-axisymmetric fibres in turbulent channel flow. *J. Fluid Mech.* **916**, A3.

ARCEN, B., OUCHENE, R., KHALIJ, M. & TANIÈRE, A. 2017 Prolate spheroidal particles' behavior in a vertical wall-bounded turbulent flow. *Phys. Fluids* **29** (9), 093301.

BAKER, L.J. & COLETTI, F. 2022 Experimental investigation of inertial fibres and disks in a turbulent boundary layer. *J. Fluid Mech.* **943**, A27.

BALAKUMAR, B.J. & ADRIAN, R.J. 2007 Large- and very-large-scale motions in channel and boundary-layer flows. *Phil. Trans. R. Soc.* A **365** (1852), 665–681.

BERNARDINI, M. 2014 Reynolds number scaling of inertial particle statistics in turbulent channel flows. *J. Fluid Mech.* **758**, R1.

BERNSTEIN, O. & SHAPIRO, M. 1994 Direct determination of the orientation distribution function of cylindrical particles immersed in laminar and turbulent shear flows. *J. Aerosol Sci.* **25** (1), 113–136.

BRENNER, H. 1961 The slow motion of a sphere through a viscous fluid towards a plane surface. *Chem. Engng Sci.* **16**, 242–251.

CAPONE, A., FELICE, F.D. & PEREIRA, F.A. 2021 Flow-particle coupling in a channel flow laden with elongated particles: the role of aspect ratio. *J. Mar. Sci. Engng* **9** (12), 1388.

CHALLABOTLA, N.R., ZHAO, L. & ANDERSSON, H.I. 2016 On fiber behavior in turbulent vertical channel flow. *Chem. Engng Sci.* **153**, 75–86.

CUI, Y., RAVNIK, J., HRIBERŠEK, M. & STEINMANN, P. 2018 A novel model for the lift force acting on a prolate spheroidal particle in an arbitrary non-uniform flow. Part I. Lift force due to the streamwise flow shear. *Intl J. Multiphase Flow* **104**, 103–112.

DABADE, V., MARATH, N.K. & SUBRAMANIAN, G. 2015 Effects of inertia and viscoelasticity on sedimenting anisotropic particles. *J. Fluid Mech.* **778**, 133–188.

DABADE, V., MARATH, N.K. & SUBRAMANIAN, G. 2016 The effect of inertia on the orientation dynamics of anisotropic particles in simple shear flow. *J. Fluid Mech.* **791**, 631–703.

DOTTO, D., SOLDATI, A. & MARCHIOLI, C. 2019 Deformation of flexible fibers in turbulent channel flow. *Meccanica* **55** (2), 343–356.

EINARSSON, J., CANDELIER, F., LUNDELL, F., ANGILELLA, J.R. & MEHLIG, B. 2015 Rotation of a spheroid in a simple shear at small Reynolds number. *Phys. Fluids* **27** (6), 063301.

FONG, K.O., AMILI, O. & COLETTI, F. 2019 Velocity and spatial distribution of inertial particles in a turbulent channel flow. *J. Fluid Mech.* **872**, 367–406.

FONT-MUÑOZ, J.S., JORDI, A., ANGLÈS, S. & BASTERRETXEA, G. 2015 Estimation of phytoplankton size structure in coastal waters using simultaneous laser diffraction and fluorescence measurements. *J. Plankton Res.* **37** (4), 740–751.

FRÖHLICH, K., MEINKE, M. & SCHRÖDER, W. 2020 Correlations for inclined prolates based on highly resolved simulations. *J. Fluid Mech.* **901**, A5.

GALLILY, I. & COHEN, A.-H. 1979 On the orderly nature of the motion of nonspherical aerosol particles. II. Inertial collision between a spherical large droplet and an axially symmetrical elongated particle. *J. Colloid Interface Sci.* **68** (2), 338–356.

HAPPEL, J. & BRENNER, H. 1965 *Low Reynolds Number Hydrodynamics*. Prentice-Hall.

JEFFERY, G.B. 1922 The motion of ellipsoidal particles immersed in a viscous fluid. *Proc. R. Soc. Lond.* A **102** (715), 161–179.

JIE, Y., CUI, Z., XU, C. & ZHAO, L. 2022 On the existence and formation of multi-scale particle streaks in turbulent channel flows. *J. Fluid Mech.* **935**, A18.

JIE, Y., XU, C., DAWSON, J.R., ANDERSSON, H.I. & ZHAO, L. 2019 Influence of the quiescent core on tracer spheroidal particle dynamics in turbulent channel flow. *J. Turbul.* **20** (7), 424–438.

KAFTORI, D., HETSRONI, G. & BANERJEE, S. 1995 Particle behavior in the turbulent boundary layer. I. Motion, deposition, and entrainment. *Phys. Fluids* **7** (5), 1095–1106.

KIM, J., MOIN, P. & MOSER, R. 1987 Turbulence statistics in fully developed channel flow at low Reynolds number. *J. Fluid Mech.* **177**, 133–166.

LE, H. & MOIN, P. 1991 An improvement of fractional step methods for the incompressible Navier–Stokes equations. *J. Comput. Phys.* **92**, 369–379.

LEE, M. & MOSER, R.D. 2015 Direct numerical simulation of turbulent channel flow up to $Re_\tau \approx 5200$. *J. Fluid Mech.* **774**, 395–415.

LILJEGREN, L.M. 1993 The effect of a mean fluid velocity gradient on the streamwise velocity variance of a particle suspended in a turbulent flow. *Intl J. Multiphase Flow* **19**, 471–484.

LUNDELL, F. & CARLSSON, A. 2010 Heavy ellipsoids in creeping shear flow: transitions of the particle rotation rate and orbit shape. *Phys. Rev.* E **81** (1), 016323.

https://doi.org/10.1017/jfm.2023.420 Published online by Cambridge University Press

LUNDELL, F., SÖDERBERG, L.D. & ALFREDSSON, P.H. 2011 Fluid mechanics of papermaking. *Annu. Rev. Fluid Mech.* **43** (1), 195–217.

MARCHIOLI, C., FANTONI, M. & SOLDATI, A. 2010 Orientation, distribution, and deposition of elongated, inertial fibers in turbulent channel flow. *Phys. Fluids* **22** (3), 033301.

MARCHIOLI, C. & SOLDATI, A. 2002 Mechanisms for particle transfer and segregation in a turbulent boundary layer. *J. Fluid Mech.* **468**, 283–315.

MARCHIOLI, C., ZHAO, L. & ANDERSSON, H.I. 2016 On the relative rotational motion between rigid fibers and fluid in turbulent channel flow. *Phys. Fluids* **28** (1), 013301.

MICHEL, A. & ARCEN, B. 2021*a* Long time statistics of prolate spheroids dynamics in a turbulent channel flow. *Intl J. Multiphase Flow* **135**, 103525.

MICHEL, A. & ARCEN, B. 2021*b* Reynolds number effect on the concentration and preferential orientation of inertial ellipsoids. *Phys. Rev. Fluids* **6** (11), 114305.

MORTENSEN, P.H., ANDERSSON, H.I., GILLISSEN, J.J.J. & BOERSMA, B.J. 2008*a* Dynamics of prolate ellipsoidal particles in a turbulent channel flow. *Phys. Fluids* **20** (9), 093302.

MORTENSEN, P.H., ANDERSSON, H.I., GILLISSEN, J.J.J. & BOERSMA, B.J. 2008*b* On the orientation of ellipsoidal particles in a turbulent shear flow. *Intl J. Multiphase Flow* **34** (7), 678–683.

NASO, A., JUCHA, J., LÉVÊQUE, E. & PUMIR, A. 2018 Collision rate of ice crystals with water droplets in turbulent flows. *J. Fluid Mech.* **845**, 615–641.

OUCHENE, R., KHALIJ, M., ARCEN, B. & TANIÈRE, A. 2016 A new set of correlations of drag, lift and torque coefficients for non-spherical particles and large Reynolds numbers. *Powder Technol.* **303**, 33–43.

OUCHENE, R., POLANCO, J.I., VINKOVIC, I. & SIMOËNS, S. 2018 Acceleration statistics of prolate spheroidal particles in turbulent channel flow. *J. Turbul.* **19** (10), 827–848.

PARSA, S., CALZAVARINI, E., TOSCHI, F. & VOTH, G.A. 2012 Rotation rate of rods in turbulent fluid flow. *Phys. Rev. Lett.* **109** (13), 134501.

PARSHEH, M., BROWN, M.L. & AIDUN, C.K. 2005 On the orientation of stiff fibres suspended in turbulent flow in a planar contraction. *J. Fluid Mech.* **545**, 245–269.

PICANO, F., SARDINA, G. & CASCIOLA, C.M. 2009 Spatial development of particle-laden turbulent pipe flow. *Phys. Fluids* **21** (9), 093305.

RAVNIK, J., MARCHIOLI, C. & SOLDATI, A. 2018 Application limits of Jeffery's theory for elongated particle torques in turbulence: a DNS assessment. *Acta Mech.* **229** (2), 827–839.

ROBINSON, S.K. 1991 The kinetics of turbulent boundary layer structure. PhD thesis, Stanford University, Stanford, CA.

SANJEEVI, S.K.P., KUIPERS, J.A.M. & PADDING, J.T. 2018 Drag, lift and torque correlations for non-spherical particles from stokes limit to high Reynolds numbers. *Intl J. Multiphase Flow* **106**, 325–337.

SHAIK, S., KUPERMAN, S., RINSKY, V. & VAN HOUT, R. 2020 Measurements of length effects on the dynamics of rigid fibers in a turbulent channel flow. *Phys. Rev. Fluids* **5** (11), 114309.

SHAPIRO, M. & GOLDENBERG, M. 1993 Deposition of glass fiber particles from turbulent air flow in a pipe. *J. Aerosol Sci.* **24** (1), 65–87.

SIEWERT, C., KUNNEN, R.P.J., MEINKE, M. & SCHRÖDER, W. 2014*a* Orientation statistics and settling velocity of ellipsoids in decaying turbulence. *Atmos. Res.* **142**, 45–56.

SIEWERT, C., KUNNEN, R.P.J. & SCHRÖDER, W. 2014*b* Collision rates of small ellipsoids settling in turbulence. *J. Fluid Mech.* **758**, 686–701.

TIMMERMANS, L.J.P., MINEV, P.D. & VAN DE VOSSE, F.N. 1996 An approximate projection scheme for incompressible flow using spectral elements. *Intl J. Numer. Meth. Fluids* **22** (7), 673–688.

VINKOVIC, I., DOPPLER, D., LELOUVETEL, J. & BUFFAT, M. 2011 Direct numerical simulation of particle interaction with ejections in turbulent channel flows. *Intl J. Multiphase Flow* **37** (2), 187–197.

VOTH, G.A. & SOLDATI, A. 2017 Anisotropic particles in turbulence. *Annu. Rev. Fluid Mech.* **49** (1), 249–276.

VREMAN, A.W. & KUERTEN, J.G.M. 2014 Comparison of direct numerical simulation databases of turbulent channel flow at $Re_\tau = 180$. *Phys. Fluids* **26** (1), 015102.

VAN WACHEM, B., ZASTAWNY, M., ZHAO, F. & MALLOUPPAS, G. 2015 Modelling of gas–solid turbulent channel flow with non-spherical particles with large stokes numbers. *Intl J. Multiphase Flow* **68**, 80–92.

WALLACE, J.M., ECKELMANN, H. & BRODKEY, R.S. 1972 The wall region in turbulent shear flow. *J. Fluid Mech.* **54**, 39–48.

WANG, G. & RICHTER, D.H. 2019 Two mechanisms of modulation of very-large-scale motions by inertial particles in open channel flow. *J. Fluid Mech.* **868**, 538–559.

YUAN, W., ZHAO, L., CHALLABOTLA, N.R., ANDERSSON, H.I. & DENG, J. 2018 On wall-normal motions of inertial spheroids in vertical turbulent channel flows. *Acta Mech.* **229** (7), 2947–2965.

https://doi.org/10.1017/jfm.2023.420 Published online by Cambridge University Press

ZASTAWNY, M., MALLOUPPAS, G., ZHAO, F. & VAN WACHEM, B. 2012 Derivation of drag and lift force and torque coefficients for non-spherical particles in flows. *Intl J. Multiphase Flow* **39**, 227–239.

ZHANG, H., AHMADI, G., FAN, F.-G. & MCLAUGHLIN, J.B. 2001 Ellipsoidal particles transport and deposition in turbulent channel flows. *Intl J. Multiphase Flow* **27** (6), 971–1009.

ZHAO, L., ANDERSSON, H.I. & GILLISSEN, J.J.J. 2013 Interphasial energy transfer and particle dissipation in particle-laden wall turbulence. *J. Fluid Mech.* **715**, 32–59.

ZHAO, L., CHALLABOTLA, N.R., ANDERSSON, H.I. & VARIANO, E.A. 2015*b* Rotation of nonspherical particles in turbulent channel flow. *Phys. Rev. Lett.* **115** (24), 244501.

ZHAO, L., CHALLABOTLA, N.R., ANDERSSON, H.I. & VARIANO, E.A. 2019 Mapping spheroid rotation modes in turbulent channel flow: effects of shear, turbulence and particle inertia. *J. Fluid Mech.* **876**, 19–54.

ZHAO, F., GEORGE, W.K. & VAN WACHEM, B.G.M. 2015*a* Four-way coupled simulations of small particles in turbulent channel flow: the effects of particle shape and stokes number. *Phys. Fluids* **27** (8), 083301.

ZHAO, L., MARCHIOLI, C. & ANDERSSON, H.I. 2014 Slip velocity of rigid fibers in turbulent channel flow. *Phys. Fluids* **26** (6), 063302.

https://doi.org/10.1017/jfm.2023.420 Published online by Cambridge University Press